Astronomy & Astrophysics manuscript no. main
February 26, 2024

The giant outburst of EXO 2030+375

II: Broadband spectroscopy and evolution

R. Ballhausen[1,2], P. Thalhammer[3], P. Pradhan[4,5], E. Sokolova-Lapa[3], J. Stierhof[3], K. Pottschmidt[6,2], J. Wilms[3], J.B. Coley[7,2], P. Kretschmar[8], F. Fürst[8], P. Becker[9], B. West[10], C. Malacaria[11], M.T. Wolff[12], R. Rothschild[13], and R. Staubert[14]

[1] University of Maryland College Park, Department of Astronomy, College Park, MD 20742, USA
[2] CRESST and NASA Goddard Space Flight Center, Astrophysics Science Division, 8800 Greenbelt Road, Greenbelt, MD 20771, USA
[3] Dr. Karl Remeis-Observatory & ECAP, Universität Erlangen-Nürnberg, 96049 Bamberg, Germany
[4] Department of Physics and Astronomy, Embry-Riddle Aeronautical University, 3700 Willow Creek Road, Prescott, AZ 86301, USA
[5] Massachusetts Institute of Technology, Kavli Institute for Astrophysics and Space Research, 70 Vassar St., Cambridge, MA 02139, USA
[6] University of Maryland Baltimore County, 1000 Hilltop Circle, Baltimore, MD 21250, USA
[7] Department of Physics and Astronomy, Howard University, Washington, DC 20059, USA
[8] ESA/ESAC, Camino Bajo del Castillo s/n, 28692, Villanueva de la Cañada, Madrid, Spain
[9] George Mason University, Fairfax, VA 22030, USA
[10] Department of Physics, United States Naval Academy, Annapolis, MD 21402, USA
[11] International Space Science Institute, Hallerstrasse 6, 3012 Bern, Switzerland
[12] Space Science Division, U.S. Naval Research Laboratory, Washington, DC 20375–5352, USA
[13] Department of Astronomy and Astrophysics, University of California San Diego, 9500 Gilman Dr., La Jolla, CA 92093, USA
[14] Institut für Astronomie und Astrophysik, Eberhard-Karls-Universität Tübingen, Sand 1, 72076 Tübingen, Germany

RECEIVED: ACCEPTED:

ABSTRACT

In 2021, the High-mass X-ray Binary EXO 2030+375 underwent a giant X-ray outburst, the first since 2006, which reached a peak flux of ~600 mCrab (3–50 keV). The goal of this work is to study the spectral evolution over the course of the outburst, search for possible cyclotron resonance scattering features (CRSFs), and to associate spectral components with the emission pattern of the accretion column. We use broadband spectra taken with *NuSTAR*, *NICER*, and *Chandra* near the peak and during the decline phase of the outburst. We describe the data with established empirical continuum models and perform pulse-phase-resolved spectroscopy. We compare the spectral evolution with pulse phase with a proposed geometrical emission model. We find a significant spectral hardening toward lower luminosity, a behavior that is expected for super-critical sources. The continuum shape and evolution cannot be described by a simple powerlaw model with exponential cutoff but requires additional absorption or emission components. We can confirm the presence of a narrow absorption feature at ~10 keV in both *NuSTAR* observations. The absence of harmonics question the interpretation of this feature as a CRSF. The empirical spectral components cannot be directly associated with identified emission components from the accretion column.

1. Introduction

The Be X-ray binary EXO 2030+375 was discovered in 1985 during a strong X-ray outburst at a 2–30 keV flux level of ~700 mCrab (Parmar et al. 1985) and soon after identified as neutron star binary with a Be companion (Motch & Janot-Pacheco 1987). In addition to its ~42 s rotation period, it is strongly variable on a wide range of timescales, including a ~200 mHz QPO (Angelini et al. 1989) and episodic flaring (Klochkov et al. 2011). EXO 2030+375 exhibits regular type I outbursts associated with its periastron passage according to its ~46 d orbit (Wilson et al. 2008). Since its discovery, in addition to the 1985 outburst, only two mode "giant" type II outbursts exceeding ~500 mCrab (3–50 keV) have been observed, in 2006 and 2021. EXO 2030+375 has an extensive observing history that provided evidence for strong neutral and ionized absorption, soft emission components, and strong pulse-phase variability. Distance estimates are still uncertain. The extinction-based estimate of 7.1 ± 0.2 kpc (Wilson et al. 2002) has recently been challenged by *Gaia* observations which find a much shorter parallax distance of $2.4^{+0.5}_{-0.4}$ kpc (Bailer-Jones et al. 2021).

The presence of a CRSF for this source is subject of active debate. The first indication for a CSRF was presented by Reig & Coe (1999) who analyzed a series of *RXTE* observations. These authors found an absorption-like feature around ~ 36 keV in the combined pulse-phase-averaged High Energy X-ray Timing Experiment (HEXTE) spectrum. The pulse-phase-resolved spectra did not allow for the detection of this feature. Reig & Coe (1999) note that they are unable to make a definitive statement about the nature of this feature. A 10 keV absorption feature was first detected in *INTEGRAL* observations of the 2006 outburst by Klochkov et al. (2007) who also found indications of a harmonic feature around 20 keV, in principle supporting an interpretation as a CRSF. However, Klochkov et al. also present an equally acceptable description of the spectrum with a broad emission line at ~13–15 keV instead of two absorption features and cau-

Table 1: Log of all observations used in this work.

ObsID	start date	net exposure [ks]
NuSTAR		
80701320002	2021-Aug-30	32.5[a]
90701336002	2021-Nov-08	23.5[a]
NICER		
4201960113	2021-Aug-30	2.3
4201960150	2021-Nov-08	15.4
Chandra		
26154	2021-Oct-20	9.7[b]

Notes. [(a)] Per Focal Plane Module. [(b)] Medium Energy Grating order +1.

tion that a CRSF detection is by no means conclusive. Wilson et al. (2008) confirmed the presence of an absorption feature near 10 keV in *RXTE* observations of the 2006 giant outburst. Most recently, Tamang et al. (2022) presented an analysis of *NuSTAR* data also used in this work that further supports the presence of this feature. Klochkov et al. (2008) revisited *INTEGRAL* data of the 2006 giant outburst and found indications of an absorption line at ~63 keV. This feature, however, does only appear in a narrow pulse phase interval.

EXO 2030+375 has been monitored extensively at various luminosity stages and with all major X-ray missions. The evolution of the broad-band spectrum has been presented by Wilson et al. (2008) and Epili et al. (2017) and has been extended down to the propeller regime by Fürst et al. (2017) and Jaisawal et al. (2021). In 2021 July, EXO 2030+375 went into its third and most recent to date giant X-ray outburst. In this paper we focus on an in-depth spectral analysis of the *NuSTAR* data taken near the peak in the decline phase of the outburst, connecting our results to the characteristic pulse profile evolution which is presented by Thalhammer et al. (2023, hereafter Paper I).

The remainder of the paper is structured as follows: In Sect. 2 we describe the data acquisition with *NICER* and *NuSTAR* over the course of the outburst and give details of the data reprocessing. In Sect. 3 and 4 we turn to detailed pulse-phase-averaged and pulse-phase-resolved spectral analysis. We discuss our results in Sect. 5 and give an outlook in Sect. 6.

2. Data Acquisition and Reduction

2.1. Monitoring of the 2021 giant outburst of EXO 2030+375

The 2021 giant outburst of EXO 2030+375 was closely monitored with *NICER* and *Swift*/XRT (see Fig. 1 for the Swift/BAT light curve). The monitoring campaign was complemented by pointed *NuSTAR* observations, once near the peak at a 3–50 keV flux of ~600 mCrab (ObsID: 80701320002; hereafter Obs. I) and during the decline phase around 250 mCrab (ObsID: 9070133600; hereafter Obs. II). The scheduling of the *NuSTAR* observations was motivated by a characteristic transition in the pulse profile and hardness ratio that had been reported in previous outbursts and was again observed through the dense *NICER* and *Swift*/XRT monitoring (Paper I, Thalhammer et al. 2021; Pradhan et al. 2021). Furthermore, the 2021 giant outburst of EXO 2030+375 was observed by *Chandra*, *AstroSAT*, and *Insight*-HXMT (Fu et al. 2023).

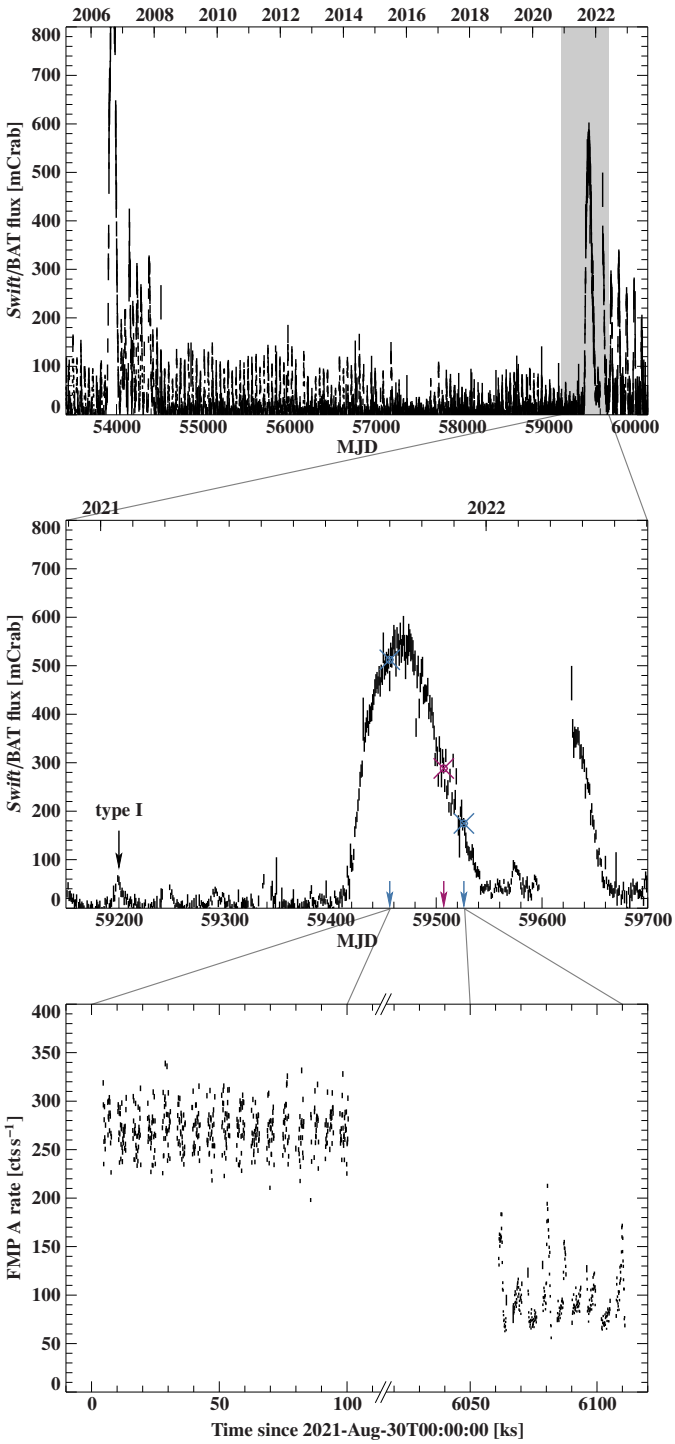

Fig. 1: *Top:* Long-term *Swift*/BAT light curve of the giant 2022 outburst of EXO 2030+375 (Krimm et al. 2013). *Middle:* Close-up of the 2021 giant outburst. Blue crosses mark the times of the *NuSTAR* observations, the magenta cross marks the time of the *Chandra* observation. *Bottom: NuSTAR* 3–78 keV lightcurve of Obs. I and II with 100 s time resolution.

2.2. NuSTAR

The NASA Small Explorer Mission *NuSTAR* (Harrison et al. 2013), launched on 2012 June 13, carries two co-aligned grazing incidence X-ray telescopes, which focus X-rays on the two focal plane modules, FPMA and FPMB. It provides a usable energy

range of 3–79 keV with a field of view of 13′×13′at 10 keV. *NuSTAR*'s imaging capabilities allow for simultaneous background determination while the pixelated CdZnTe detectors do not suffer from pile-up for count rates up to 10^5 cts s^{-1} pixel^{-1}.

We reprocessed the data of both *NuSTAR* observations with the standard `NUSTARDAS` pipeline version 2.0.0 with CalDB version 20211020. The source and background regions for both observations are circles of 90″radius, centered on the source and in the opposite corner of the field of view, respectively, to avoid contamination with source photons. We note that even at around 60 keV the source count rate is still about an order above the background rate, so systematic effects of measuring the background on a different chip are expected to be negligible. Our screening results in ∼32 ks cleaned exposure per FPM for Obs. I and ∼23 ks for Obs. II. Event times were converted to the solar barycenter.

2.3. NICER

The Neutron star Interior Composition Explorer (*NICER*; Gendreau et al. 2016) was installed on the International Space Station in 2017. Its X-ray Timing Instrument (XTI) consists of 56 X-ray "concentrator" optics in combination with silicon detectors. Unlike *NuSTAR*, the XTI is not an imaging instrument, so background rates have to be reconstructed from models. *NICER* features timing resolution of 300 ns with a large collecting area over a bandpass of 0.2–12 keV.

Out of the extensive *NICER* monitoring data, which is analyzed and presented in detail in Paper I, we only use those observations contemporaneous with *NuSTAR* to extend soft coverage (ObsID 4201960113 with *NuSTAR* Obs. I with a net exposure of ∼2.3 ks and ObsID 4201960150 for *NuSTAR* Obs. II with a net exposure of ∼15.4 ks). Data reduction follows standard procedures using the *NICER* data analysis pipeline of Heasoft version 6.31.1 with CALDB version 20220413. We use the `SCORPEON` background model[1]. A detailed description of the data reduction is given in Paper I.

2.4. Chandra

The Chandra X-Ray Observatory consists of the High Energy Transmission Grating Spectrometer (HETGS) with a medium-energy grating (MEG; 0.4–5.0 keV), and a high-energy grating (HEG; 0.8–10.0 keV). The HETGS have resolving powers up to about 1000 and effective area up to about 150 cm^2. The dispersed grating spectra are recorded with an array of CCDs (Advanced CCD Imaging Spectrometer, ACIS-S; Garmire et al. 2003). We requested DDT observations of the source near the peak of the outburst, but owing to a problem with the insertion of the low energy grating around that time, we obtained grating observations of the source for 10 ks in FAINT TIMED mode only around 2021-Oct-20 (ObSID 26154), when the source was already in decline. The counts spectra for the observations were extracted using `TGCat` reprocessing scripts (Huenemoerder et al. 2011), using CIAO (Fruscione et al. 2006) version 4.8 and Calibration Database version 4.7.2.

3. Pulse-phase-averaged spectroscopy

We examined the *NuSTAR* lightcurves in various energy bands over the course of the respective observations. The lightcurve of Obs. I is rather stable, while Obs. II exhibits strong flaring activity on ks timescales (see Fig. 1). If we compare variability of the hardness ratios over a range of energy bands with the lightcurves, however, they appear remarkably constant in both observations, indicating no significant spectral variability over the course of the individual observations. This behavior allows us to begin our spectral analysis from time- and pulse-phase averaged spectra where we expect the spectral shape to be only dependent on the luminosity.

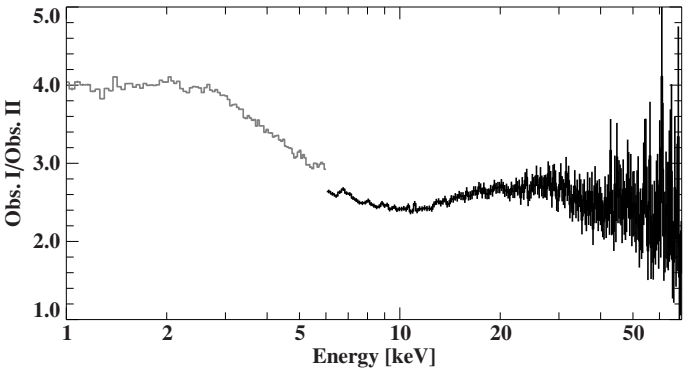

Fig. 2: Energy-resolved count rate ratio of Obs. I over Obs. II. The gray curve is *NICER*/XTI; the black is *NuSTAR*/FPMA. The offset between *NICER* and *NuSTAR* points at flux cross-calibration uncertainties between the instruments.

In a first step we investigate the spectral change from one observation to the other in a model-independent way by calculating energy-resolved ratios of the count rates of both observations in *NICER* and *NuSTAR* (see Fig. 2). We find Obs. I to be significantly softer than Obs. II, with a prominent excess of emission mostly below ∼5 keV. However, we note that the spectral evolution from Obs. I to Obs. II is more complex than can be fully captured by spectral hardness and distinct differences in spectral shape become apparent over the full *NuSTAR* energy range.

We use `isis` v.1.6.2-51 (Houck & Denicola 2000) for spectral fitting. For spectral fitting we rebin the data according to the optimal binning scheme of Kaastra & Bleeker (2016), but requiring at least 25 counts per spectral bin. We note a significant mismatch between *NICER* and *NuSTAR* between 6 keV and 10 keV, which is likely due to cross-calibration issues, so we use an energy range of 1–6 keV for *NICER* and 4.5–78 keV for *NuSTAR*. We further add a 1% systematic uncertainty for the *NICER* data to account for possible calibration uncertainties[2]. Our model includes constants for flux cross-calibration uncertainties relative to *NuSTAR*/FPMA and we fit an gainshift offset for all three instruments to account for energy calibration uncertainties around astrophysical and instrumental absorption edges. We find that permitting a slight gainshift leads to significant improvements of the fit statistic of $\Delta\chi^2 \sim 40$ for Obs. I and $\Delta\chi^2 \sim 25$ for Obs. II (for the respective best-fit model). The found gainshifts are within 1–2 RMF energy bins(*NICER*/XTI: 10 eV and *NuSTAR*/FPM: 40 eV)[3]. Uncertainties are given at the 90% confidence level unless otherwise noted and obtained by varying a single parameter of interest for a $\Delta\chi^2 = 2.71$.

[1] `https://heasarc.gsfc.nasa.gov/docs/nicer/analysis_threads/scorpeon-overview/`

[2] See *NICER* calibration memo NICER-Cal-SysErr-20221001 which estimates ∼1% systematic errors dominated by the response matrix for bright targets.

[3] The estimated uncertainties of *NuSTAR*'s and *NICER*'s energy calibration are ∼40 eV (Grefenstette et al. 2022) and a ∼5 eV (see NICER-Cal-Energy-Scale-optmv13-20221001), respectively.

Table 2: Best-fit parameters for the phase-averaged spectrum of *NuSTAR* Obs. I and II. A partial covering absorber is not required in Obs. II.

parameter	Obs. I	Obs. II
$c_{\rm FPMB}$	$0.9878^{+0.0018}_{-0.0017}$	$0.9988^{+0.0030}_{-0.0029}$
$c_{\rm XTI}$	1.032 ± 0.006	0.939 ± 0.005
$N_{\rm H,1}{}^{a}$	$3.9^{+0.8}_{-0.6}$	2.64 ± 0.03
$N_{\rm H,2}{}^{a}$	$2.15^{+0.25}_{-0.47}$	—
pcf	$0.71^{+0.18}_{-0.16}$	—
$kT_{\rm BB}{}^{b}$	$0.472^{+0.036}_{-0.028}$	2.44 ± 0.04
$F_{\rm BB}{}^{c}$	$0.58^{+0.18}_{-0.13}$	0.47 ± 0.03
Γ	$1.114^{+0.011}_{-0.012}$	1.019 ± 0.014
$E_{\rm fold}{}^{b}$	$18.22^{+0.17}_{-0.18}$	19.3 ± 0.4
$F_{\rm PL}{}^{d}$	$15.51^{+0.08}_{-0.07}$	$4.81^{+0.04}_{-0.05}$
$A_{\rm Fe}{}^{e}$	6.7 ± 0.4	$1.91^{+0.23}_{-0.21}$
$E_{\rm Fe}{}^{b}$	$6.594^{+0.023}_{-0.019}$	6.54 ± 0.05
$\sigma_{\rm Fe}{}^{b}$	$0.277^{+0.018}_{-0.017}$	0.33 ± 0.05
$E_{\rm 10\,keV}{}^{b}$	$10.23^{+0.13}_{-0.15}$	9.4 ± 0.4
$\sigma_{\rm 10\,keV}{}^{b}$	$2.58^{+0.29}_{-0.23}$	$1.8^{+0.6}_{-0.4}$
$d_{\rm 10\,keV}{}^{b}$	$0.32^{+0.06}_{-0.05}$	$0.13^{+0.10}_{-0.05}$
$\mathcal{L}^{f}$	1.1×10^{37}	3.6×10^{36}
$\rm GS_{FPMA}{}^{g}$	-29^{+15}_{-19}	-80^{+29}_{-20}
$\rm GS_{FPMB}{}^{g}$	-37^{+14}_{-18}	-75^{+27}_{-25}
$\rm GS_{XTI}{}^{g}$	-9 ± 4	$1.2^{+2.8}_{-2.7}$

Notes. [a] In $10^{22}\,\rm cm^{-2}$. [b] In keV. [c] Unabsorbed 1–10 keV flux in $10^{-9}\,\rm erg\,s^{-1}\,cm^{-2}$. [d] Unabsorbed 3–50 keV flux in $10^{-9}\,\rm erg\,s^{-1}\,cm^{-2}$. [e] Photon flux in $10^{-3}\,\rm phs\,cm^{-2}\,s^{-1}$. [f] 3–50 keV luminosity in $\rm erg\,s^{-1}$ for a distance of 2.4 kpc. [g] Additive gainshift in eV.

Our continuum model is based on earlier analyses of EXO 2030+375 (e.g., Klochkov et al. 2011) and consists of an absorbed powerlaw with exponential folding and a blackbody component. We use the abundances for the interstellar medium from Wilms et al. (2000) and the cross sections of Verner et al. (1996) to model neutral photoelectric absorption. Also based on previous observations(e.g., Naik et al. 2013; Ferrigno et al. 2016), we also include a partial covering absorber distribution in order to model absorption in the binary system. The Fe Kα complex is described by a broad Gaussian emission line in *NuSTAR* Obs. I and II.

We found the inclusion of the 10 keV absorption feature (`gabs` in `isis/xspec`; absorption line with Gaussian optical depth) mentioned above to result in the largest improvement in χ^2, namely from 1256.32 to 741.76 for Obs. I, and 713.14 to 657.37 for Obs. II, while the χ^2 improvement for the 36 keV feature in Obs. I was only $\Delta\chi^2 = 11.92$. We note that the temperature of the blackbody component increases by roughly a factor of five from Obs. I to Obs. II. This component rather appears to be a broad contribution to the moderately hard emission resembling the "10-keV-feature" seen in emission in several other pulsars (e.g., 4U 0115+63). The blackbody emission component in Obs. II roughly peaks at the location of the 10 keV absorption feature. The best-fit parameters are listed in Table 2 and Fig. 3 shows the respective spectra with best-fit model and residuals. In `isis/xspec` notation, our full model is

$$S(E) = \texttt{detconst}\times\texttt{tbabs}\times(\texttt{bbody}+\texttt{cutoffpl}+\texttt{egauss})*\texttt{gabs}\,,$$

where for Obs. II the partial covering fraction is unity as for a homogeneous absorber.

Interestingly, if line-like absorption features are included in Obs. II, a partial covering absorber does not significantly improve the fit. We also note that the requirement of a partial covering absorber in Obs. I is mostly based on a soft excess below ~2 keV in *NICER*/XTI which may be subject to further calibration uncertainties or inadequate background modeling or unaccounted emission components in our current model. We therefore conclude that there is no strong support for a partial covering absorber from broadband continuum absorption or edge absorption and other possible interpretations include a partially ionized absorber that cannot be resolved with *NICER* and *NuSTAR*. The Fe K emission complex indicates a certain degree of ionization due to its width and centroid energy. Our best-fit model therefore includes a partial absorber component only for Obs. I.

For spectral fitting of the *Chandra* HETG data we combined orders +1 and −1 of MEG and HEG, respectively and rebinned the data to a signal-to-noise ratio of 25, 5, and 10 in the respective energy bands 1–6 keV, 6–7 keV, and 7–10 keV. We only fit the 1–10 keV spectrum and use *C*-statistics (Cash 1979) for this dataset because of its lower statistic and our focus on weak line features. Due to lack of hard X-ray coverage at the time of the *Chandra* observation, we find a continuum model used in Paper I, consisting of an absorbed powerlaw with an additional blackbody sufficient. The pure continuum model resulted in a best-fit statistic of *C*-stat/d.o.f. of 542.82/426 = 1.27.

Upon visual inspection of MEG and HEG spectra (see Fig. 4) we do not notice the presence of strong absorption or emission lines. We expect at least a significant iron line emission, as the analysis of the *NICER* monitoring data consistently found Fe K emission lines with equivalent widths of the order of a few tens of eV. While the Fe K band emission in *NICER* appears a broad feature, we expect to find the neutral and highly ionized lines well resolved in the grating spectra. In order to constrain limits on the expected emission lines we added four narrow Gaussian lines at the energies of Si XIV Lyα, Fe Kα, Fe XXV Heα, and Fe XXVI Lyα (2.41 keV, 6.40 keV 6.70 keV, and 6.97 keV) with their width fixed at 10 eV. Adding those features improves the fit to *C*-stat/d.o.f. of 510.80/422 = 1.21, although the lines still appear very weak. The best-fit parameters are given in Table 3. The most striking result of the *Chandra* observation is that the low Fe K line flux does not seem to be consistent with the *NICER* observations. We note that the *NICER* monitoring also indicated a moderate variability of the Fe line equivalent width and it is possible that the *Chandra* observation happened to catch an episode of very low line emission. Additionally, some of the observed Fe K line flux in *NICER* may result from blended, unresolved intermediate ionization states. Due to *Chandra*'s lower collecting area, these enhanced emission lines will be more difficult to disentangle from the underlying continuum. We note that Fe K line emission in *NICER* is best fit with a broad Gaussian with a centroid energy between neutral Fe I and Fe XXV which supports the idea of a wide range of ionization states.

Possible absorption features that are reported in the literature that might be associated with a CRSF are at ~10 keV (Klochkov et al. 2007), ~36 keV (Reig & Coe 1999) and ~63 keV (Klochkov et al. 2008). We therefore tested how much adding those absorption features improved the fit. We only found a slight improvement when including a 36 keV line in Obs. I, otherwise only upper limits on the line strength can be given (see Table 4). For testing the presence of these lines, we kept the line widths fixed at conventional values (note that Reig & Coe 1999

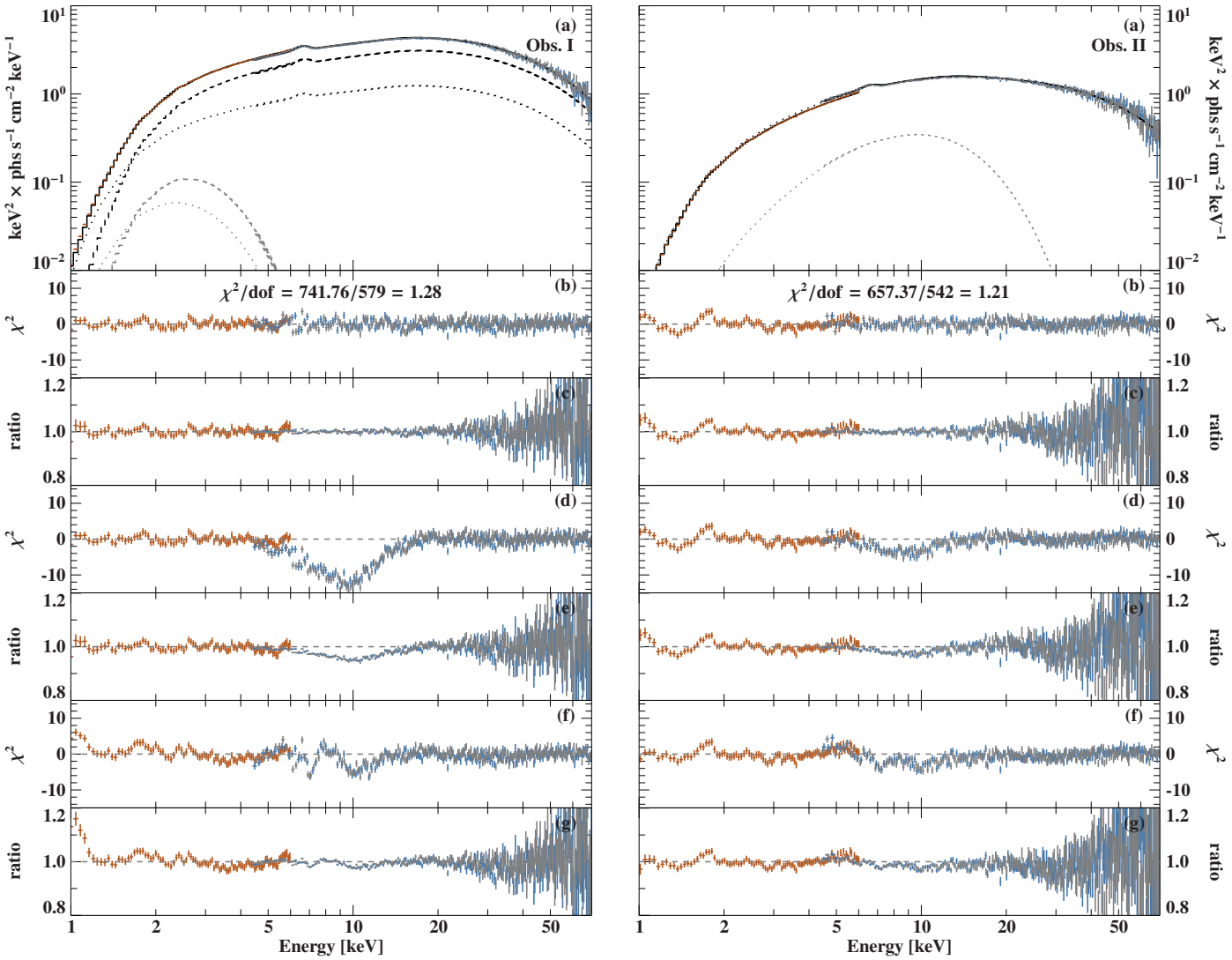

Fig. 3: Panel a: pulse-phase-averaged νF_ν spectrum Obs. I (*left*) and Obs. II (*right*) of EXO 2030+375 with best-fit absorbed cut off power law model for *NuSTAR*/FPMA (gray), FPMB (blue), *NICER*/XTI (orange). Panels b and c: residuals and ratio for the best-fit model. The black dashed and dotted lines show the individual partial covering continuum components. The gray dashed and dotted lines show the partially absorbed blackbody component only. Panels d and e: residuals and ratio for the model evaluated without the 10 keV absorption feature. Panels f and g: residuals and ratio for the model re-fitted without the 10 keV absorption feature.

using a Lorentzian report a width of 1 keV of the 36 keV feature) but let the centroid energy free within a very narrow range since CRSF energies are known to vary with time and luminosity (Staubert et al. 2019).

4. Pulse-phase-resolved spectroscopy

EXO 2030+375 is known for the significant variability of its pulse profile with luminosity and the *NuSTAR* observations aimed at capturing broadband spectral transitions associated with the pulse profile evolution. The pulse profile evolution as observed with *NICER* was presented in Paper I. We obtained the pulse period at the time of the *NuSTAR* observations by epoch folding barycentered, dead-time corrected lightcurves with 0.5 s binning. The resulting broad-band pulse profiles and pulse-phase-resolved hardness ratios are shown in Fig. 5. The pulse profile transition reported by *NICER* and *Swift* is characterized by a change in the relative intensity of the observed pulses around $\phi = 1.0$ and $\phi = 1.3$, respectively (as defined in Fig. 5 and Paper I). In addition to the sharp feature at ϕ~0.75 reported in Paper I, the pulse-phase-resolved hardness ratio shows a dramatic change around the dip at $\phi = 1.1$–1.2, which is softer than the neighboring peaks in Obs. I, but harder in Obs. II.

The pulse-phase-resolved hardness ratios do not only indicate a variation of spectral shape with luminosity, but also with rotational phase of the neutron star. This latter variation changes strikingly between the two observations. We therefore performed pulse-phase-resolved spectroscopy of the data of both *NuSTAR* observations to study the nature of this variability in more detail. Our selection of phase intervals (e.g., Fig. 6) aims at capturing all significant changes in hardness ratios of several different energy bands while maintaining sufficient signal-to-noise in each phase interval to obtain meaningful parameter constraints.

The model used for fitting the pulse-phase-resolved spectra is the same as for the pulse-phase-averaged data, but we fix the gainshift and *NuSTAR*/FPMB flux constant at the values found in Sect. 3. Our initial fits further showed a degeneracy between the absorption column and the blackbody parameters so we also

Table 3: Best-fit parameters for the *Chandra*/HETG spectrum of EXO 2030+375. All line widths were fixed to 10 eV.

parameter	value
$N_{\rm H}{}^{a}$	$2.26^{+0.06}_{-0.07}$
$F_{\rm PL}{}^{b}$	4.49 ± 0.03
Γ	$1.05^{+0.06}_{-0.05}$
$kT_{\rm BB}{}^{c}$	$0.63^{+0.04}_{-0.06}$
$F_{\rm BB}{}^{b}$	0.28 ± 0.02
$E_{\rm Si\,XIV\,Ly\alpha}{}^{c}$	$2.41^{\dagger}$
$A_{\rm Si\,XIV\,Ly\alpha}{}^{d}$	$0.74^{+0.29}_{-0.30}$
$E_{\rm Fe\,K\alpha}{}^{c}$	$6.40^{\dagger}$
$A_{\rm Fe\,K\alpha}{}^{d}$	$0.27^{+0.22}_{-0.18}$
$E_{\rm Fe\,XXV\,He\alpha}{}^{c}$	$6.70^{\dagger}$
$A_{\rm Fe\,XXV\,He\alpha}{}^{d}$	$0.42^{+0.25}_{-0.24}$
$E_{\rm Fe\,XXVI\,Ly\alpha}{}^{c}$	$6.97^{\dagger}$
$A_{\rm Fe\,XXVI\,Ly\alpha}{}^{d}$	< 0.38

Notes. [(a)] In 10^{22} cm^{-2}. [(b)] Unabsorbed 0.1–10 keV flux in 10^{-9} erg s^{-1} cm^{-2}. [(c)] In keV. [(d)] Photon flux in 10^{-3} phs cm^{-2} s^{-1}.

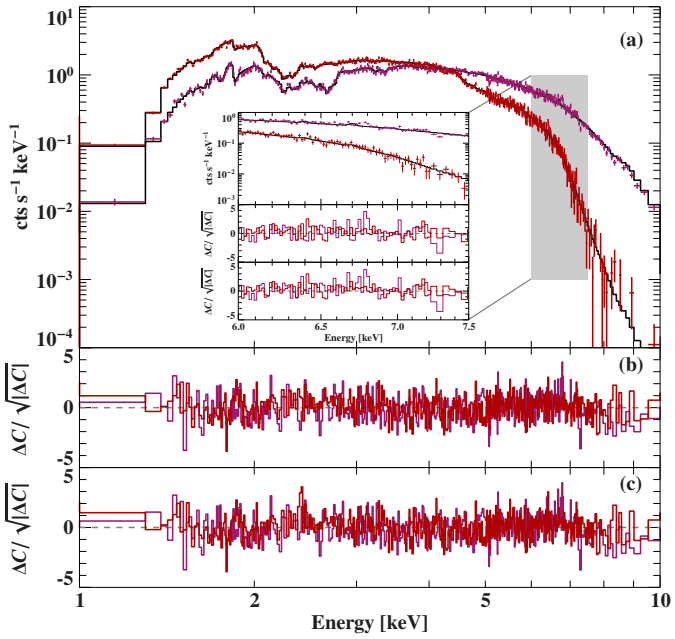

Fig. 4: *Chandra*/HETG spectrum of EXO 2030+375. Panel (a) shows the count spectrum of MEG (red) and HEG (magenta) with the best-fit model (black). The inset shows a close-up of the iron band. Panel (b) shows C residuals for the best-fit model with Si XIV Lyα, Fe Kα, Fe XXV Heα, and Fe XXVI Lyα lines. Panel (c) shows C residuals for the same best-fit continuum model without any emission lines.

Table 4: Centroid optical depth τ of absorption features at previously reported CRSF energies. Line widths have been fixed during fitting.

Energy	Width	Obs. I	Obs. II
10 keV	2.5 keV	$0.049^{+0.003}_{-0.004}$	0.038 ± 0.008
36 keV	1.0 keV	0.048 ± 0.020	≤ 0.025
63 keV	5.0 keV	≤ 0.025	≤ 0.048

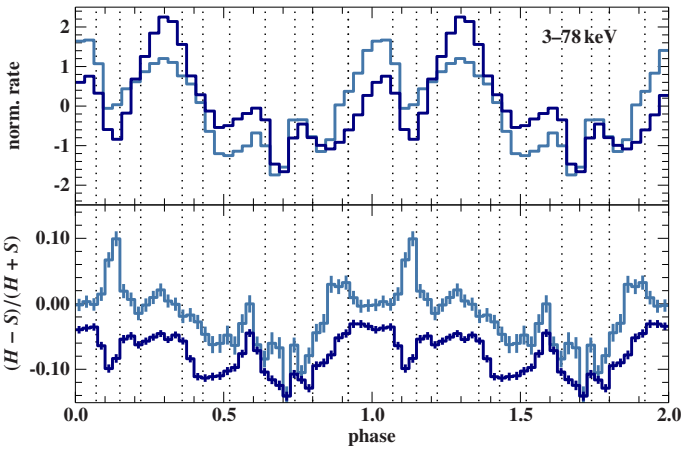

Fig. 5: *Top: NuSTAR* broadband pulse profile for Obs. I (dark blue) and Obs. II (light blue). The pulse profiles are normalized to average zero and units of standard deviation. Dotted lines mark the phase intervals selected for pulse-phase-resolved spectroscopy. *Bottom:* Hardness ratio of the 3–7 keV and 7–14 keV band, defined as $(H - S)/(H + S)$. The phase definition is the same as in Paper I.

fix $N_{\rm H}$ to the pulse-phase-averaged values for each observation. As the 10 keV feature in Obs. II is shallower and statistics are worse we further fixed its width to the pulse-phase-averaged value. In our fits we observed a slight variability of about ∼5% of the *NICER*/XTI flux constant relative to *NuSTAR*/FPMA with pulse phase. We confirmed that this behavior is a result of the much shorter *NICER*/XTI exposures and reflects pulse-pulse variability between the simultaneous and non-simultaneous segments of the *NuSTAR* observation. These changes are at a level that does not affect our overall conclusions.

The parameter evolution with pulse phase for both observation is shown in Figs. 7 and 8. While the total flux difference between the two observations is about a factor of three, the flux of the blackbody flux is barely changing with luminosity. In Obs. I, the blackbody flux contribution is almost constant, except for phase interval $\phi = 0.07$–0.15 where it roughly doubles compared to average. In Obs. II, the blackbody flux appears more variable but also peaks at a similar phase as in Obs. I. The blackbody temperature in Obs. II is constantly higher than in Obs. II, as expected from the pulse-phase-averaged fit. In Obs. I, the blackbody temperature varies moderately and roughly correlates with the main peak of the pulse profile. In Obs. II, the temperature evolution is more complex and also peaks at $\phi = 0.07$–0.15 where a spectral hardening is observed in Fig. 5. We note that a systematic effect of fixing the photoelectric absorption component for the pulse-phase-resolved fits on the blackbody temperature cannot be excluded, especially for Obs. I, where the flux of this component peaks below 2 keV.

The powerlaw continuum behaves similarly in both observations. Again, the most striking differences appear around phases $\phi = 0.07$–0.36, where the folding energy and photon index differ substantially between the observations. Overall, the powerlaw continuum parameters evolve rather smoothly.

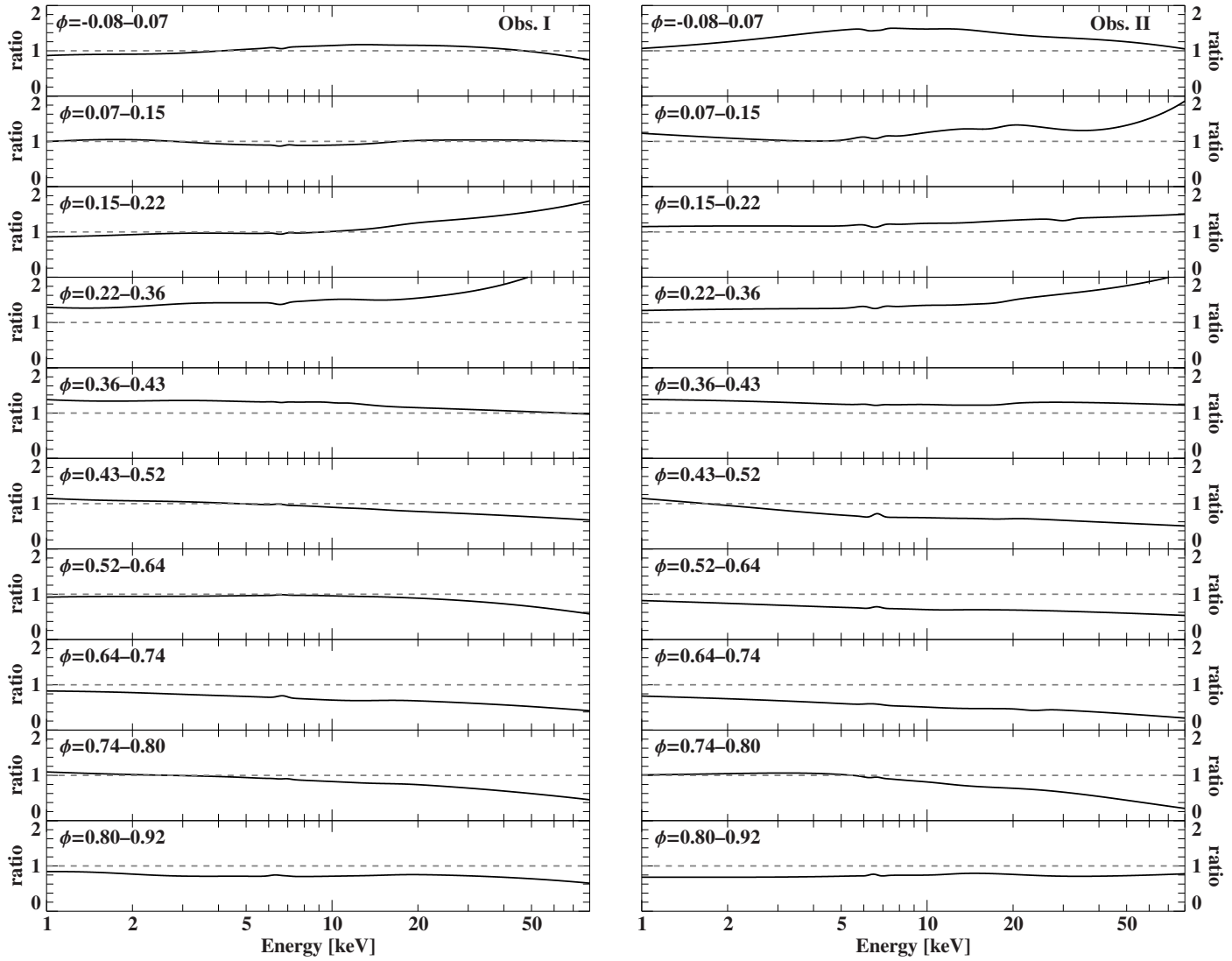

Fig. 6: Ratio plots of the best-fit pulse-phase-resolved model to the pulse-phase-averaged model.

5. Discussion

5.1. Continuum evolution with luminosity

Assuming a distance of 2.4 kpc, the inferred 3–50 keV luminosities for the times of the two *NuSTAR* observations are $\sim 1.1 \times 10^{37}$ erg s^{-1} and $\sim 3.6 \times 10^{36}$ erg s^{-1}, respectively. The luminosity is therefore comparable to the critical luminosity of $(2.3–4.6) \times 10^{36}$ erg s^{-1}, derived from the 3–30 keV flux, for the system, estimated by Epili et al. (2017) from comprehensive *RXTE* data of type I and type II outbursts of EXO 2030+375[4]. This is consistent with Epili et al., who find the spectrum to harden as the luminosity decreases for the luminosity range of the *NuSTAR* observations. We also note, however, that in Paper I (Fig. 5), the two *NuSTAR* observations clearly appear at the super-critical branch of the hardness-luminosity diagram. While there is a systematic shift in derived luminosity due to the different energy bands, it also reflects that the spectral hardening is not solely caused by a change in the powerlaw index or exponential cutoff, but rather due to a complex change in broadband spectral shape that in our model is mostly reflected by an increase of the blackbody temperature. Empirically, this hot blackbody serves as a hard broad emission component. The powerlaw flux roughly follows the evolution of the overall luminosity. Becker & Wolff (2007) propose a physically motivated spectral model of accretion powered neutron stars based solving the radiative transfer equation of the accretion column under certain assumptions. In their model, the seed photons form blackbody and cyclotron emission as well as bremsstrahlung which experience thermal and bulk Comptonization in the infalling plasma. In this picture, the spectral transition from Obs. I to II may be interpreted as a decrease of bremsstrahlung emission at lower accretion rate. Accordingly, harder blackbody emission is expected for higher impact velocities on the neutron star surface.

Postnov et al. (2015) study the spectral hardness evolution of accreting pulsars with luminosity, including EXO 2030+375 using *RXTE*/ASM data. They propose a surface reflection model to explain the hardening with luminosity that tends to saturate at intermediate luminosities of what would be few times 10^{36} erg s^{-1} for our assumed distance of 2.4 kpc[5]. Their observed hardness evolution using *RXTE*/ASM bands of 1.33–

[4] Epili et al. (2017) derive a critical luminosity of $(2–4) \times 10^{37}$ erg s^{-1} for an assumed distance of 7.1 kpc.

[5] In Postnov et al. (2015), the saturation is reported above 10^{37} erg s^{-1} but they also assume a distance of ~7 kpc.

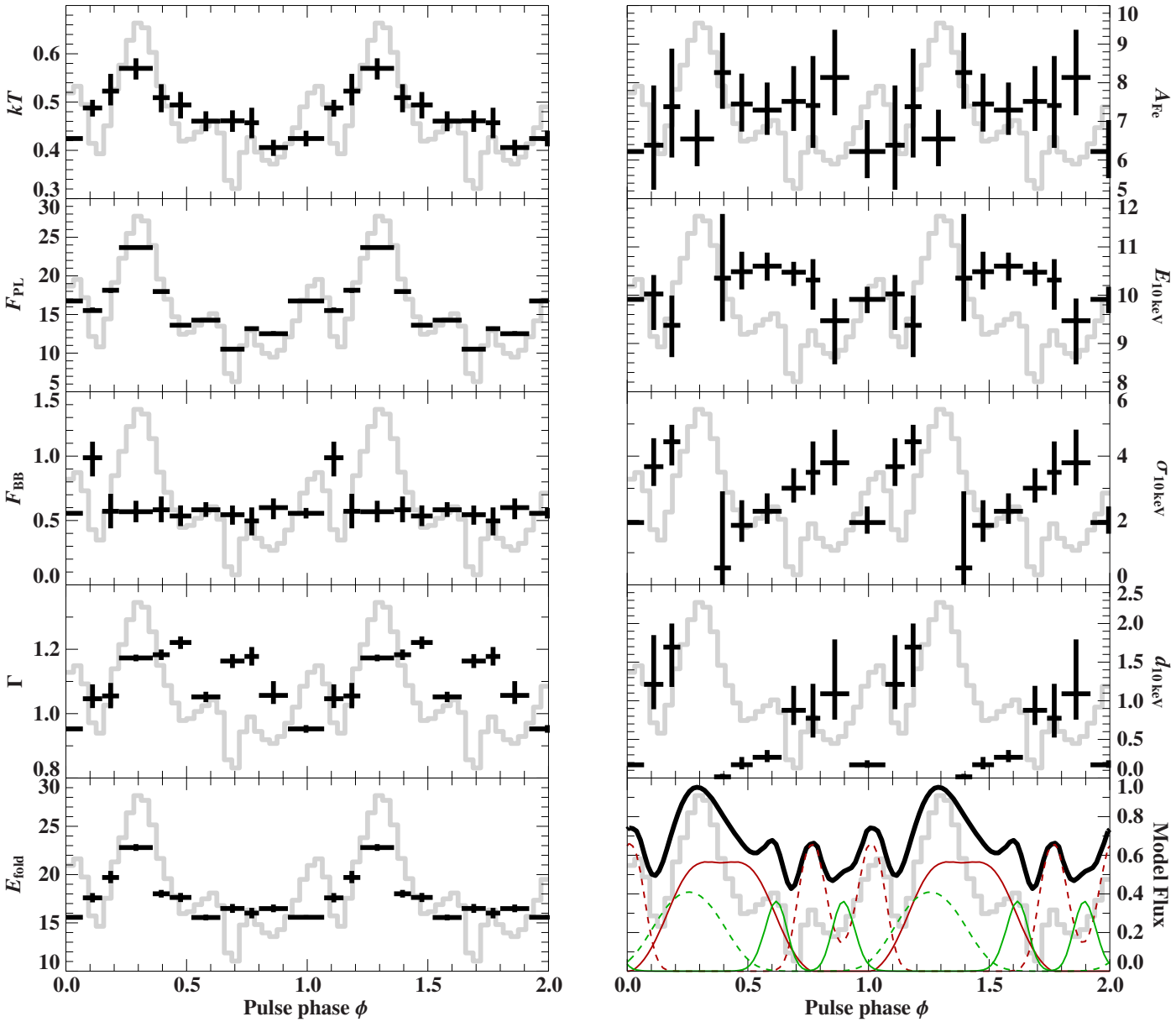

Fig. 7: Evolution of spectral model parameters with pulse phase (black) for Obs. I, along with the component-resolved column emission as presented in Paper I. The model consists of an absorbed powerlaw with exponential folding and an additional blackbody component, as well as Fe Kα emission line and an absorption feature with Gaussian optical depth (`gabs`). The free parameters (top to bottom, left to right) are: The blackbody temperature in keV, the powerlaw and blackbody fluxes in 10^{-9} erg s^{-1} cm^{-2}, the photon index, the folding energy in keV, the Fe Kα line flux in 10^{-3} photons cm^{-2} s^{-1}, the energy, width and strength of the Gaussian absorption feature in keV. The depth of the 10 keV absorption feature is consistent with zero at ϕ~0.3 and energy and width cannot be constrained. The bottom right panel shows the pulse profile model with solid and dashed line indicating wall and top emission components, respectively for the two accretion columns, and the full pulse profile in black. All panels show the 3–78 keV *NuSTAR* pulse profile of Obs. I in light gray. The pulse profile model was obtained from fitting the 3.5–4.5 keV *NICER* pulse profile of ObsID 4201960113.

3 keV and 5–12 keV contrasts the hardness ratio evolution observed by Epili et al. (2017) at the 3–10 keV and 10–30 keV bands that peaks at slightly lower luminosity. Accounting for the difference in assumed distance we find our *NuSTAR* and *NICER* hardness ratio evolution to be in agreement with the long term *RXTE*/PCA and *RXTE*/HEXTE motoring reported by Epili et al. (2017).

The complex spectral shape of the soft continuum in Obs. I cannot be modeled solely with a single absorbed powerlaw and blackbody. We find that a partial covering absorber improves the description of the soft spectrum, but without the clear detection of absorption edges, the physical interpretation of the partial covering absorber cannot be robustly confirmed. At the available spectral resolution, physical properties of the absorbing medium (e.g., ionization), or an even more complex emission spectrum, cannot be properly constrained.

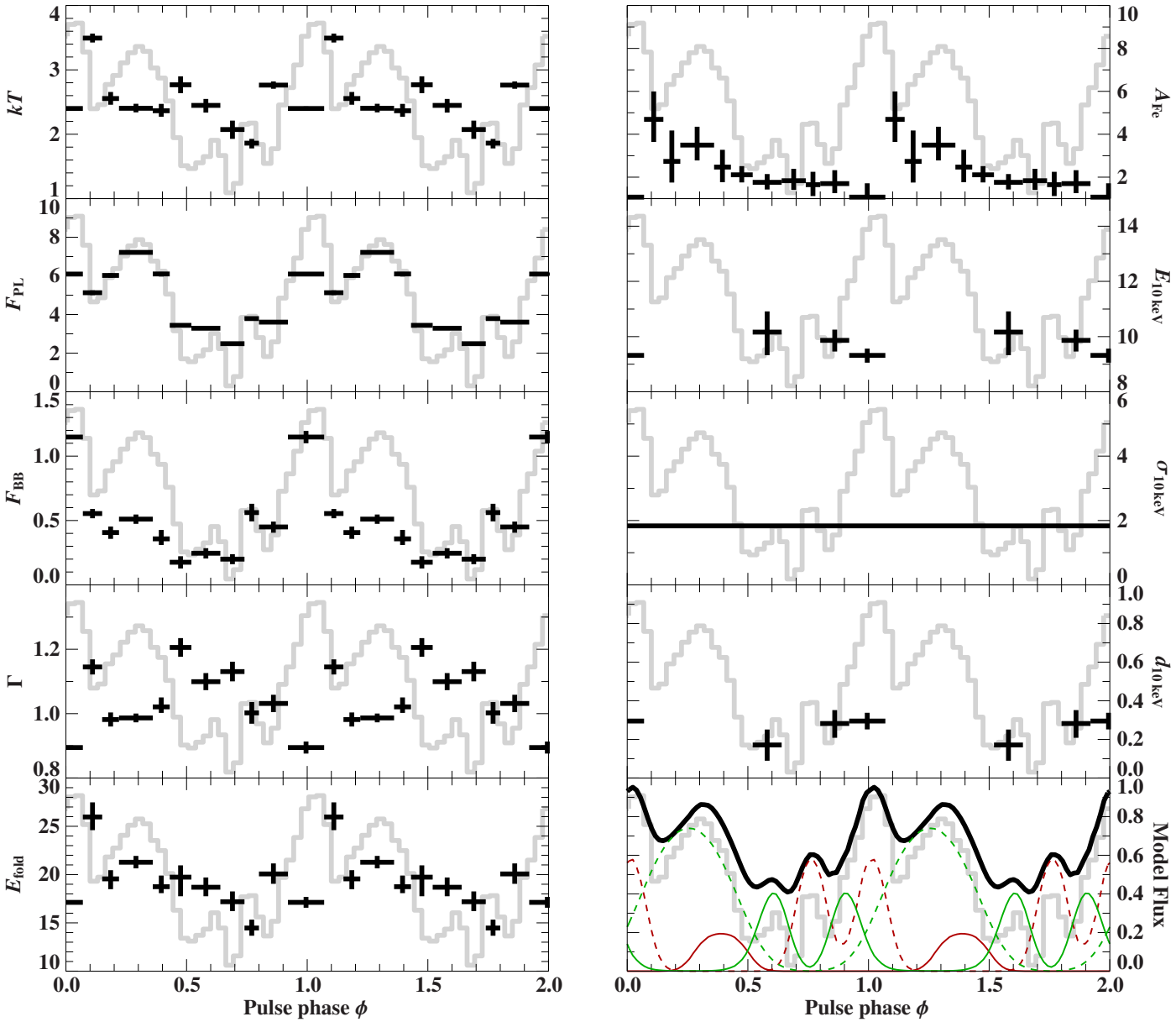

Fig. 8: Evolution of spectral model parameters with pulse phase (black) for Obs. II. Panels and units are the same as Fig. 7 but for Obs. II. The width of the 10-keV absorption feature was fixed to the pulse-phase-averaged value of 1.8 keV. Energies of 10-keV absorption feature are not shown where the depth is consistent with zero. All panels show the 3–78 keV *NuSTAR* pulse profile of Obs. II in light gray. The pulse profile model was obtained from fitting the 3.5–4.5 keV *NICER* pulse profile of ObsID 4201960150.

5.2. Absorption features

EXO 2030+375 is an actively debated CRSF candidate source with a number of potential spectral features. The first suggestion of a CRSF detection at ~36 keV was reported by Reig & Coe (1999) who observed an absorption like feature in stacked *RXTE*/HEXTE observations. Due to the known variability, the complex continuum shape, and the absence of a harmonic feature, Reig & Coe (1999) caution, however, that a definitive statement about the nature of the 36 keV feature cannot be made. In contrast to these earlier analyses, in their reanalysis of the *RXTE* data Epili et al. (2017) did not find any indications for absorption features that could be potential CRSFs in *RXTE* data.

Another possible absorption feature at ~63 keV was detected by Klochkov et al. (2008) in archival *INTEGRAL* data of the 2006 giant outburst. Klochkov et al. (2008) were only able to detect this feature during a relatively short range of pulse phase and not in the pulse-phase-averaged spectrum. The data quality further makes the assessment of the statistical significance difficult. None of the authors who analyzed the *RXTE*/HEXTE data of EXO 2030+375 report the presence of such a feature.

We tested for the presence of these absorption features but cannot confirm the presence of either the 36 kev or 63 keV lines. Adding these lines only leads to a minor improvement of the fit statistics for the 36 keV in Obs. I. We note however, that only an upper limit for the optical depth can be obtained for Obs. II which albeit fainter, still has excellent statistical quality. We further note that line energies and widths had to be fixed during the fit in order to obtain meaningful results for the optical depth. Support for these claimed CRSF detections from these two *NuSTAR* observations therefore remains tenuous at best.

The most robustly detected absorption-like feature discussed in the literature appears around ∼10 keV. It was first reported by Klochkov et al. (2007) in *INTEGRAL* spectra and later confirmed by Wilson et al. (2008) using *RXTE*, both of the 2006 giant outburst. *NuSTAR* observed the 2021 giant outburst twice and Tamang et al. (2022) report the detection of a ∼10 keV absorption feature in Obs. I, which is in line with our detection in both *NuSTAR* observations, albeit at smaller optical depth in Obs. II. While we can therefore confirm the presence of an ∼10 keV absorption-like feature, its interpretation as a CRSF remains an open question.

The most prominent CRSF source to compare with is evidently 4U 0115+63 which exhibits a fundamental CRSF at ∼11 keV (e.g., Heindl et al. 1999; Müller et al. 2013; Staubert et al. 2019; Bissinger né Kühnel et al. 2020, and references therein), and despite its complex continuum shape and variability allows for the firm detection of up to five harmonics. While the depth and width of absorption feature in the spectrum of EXO 2030+375 are comparable with those of the fundamental CRSF in 4U 0115+63, we do not find signatures of absorption features at harmonic energies of the ∼10 keV feature. Despite the many unknowns in the physical details of CRSF formation, we are not aware of a strong argument that prevent harmonic lines from forming for *B*-fields as low as a ∼10 keV fundamental (see, e.g., Schönherr et al. 2007). It is therefore very well possible that the observed absorption dip is the result of the purely empirical continuum modeling and not physical. We emphasize that similar line-like features that are not caused directly by the cyclotron resonance have been observed in a number of sources, although generally at much lower luminosity, where the spectral transition toward a two-component spectrum mimics an absorption feature between 10 keV and 20 keV on top of smooth powerlaw continuum. Examples include GX 304−1 (Tsygankov et al. 2019b), A 0535+26 (Tsygankov et al. 2019a), GRO J1008−57 (Lutovinov et al. 2021), and SRGA J124404.1−632232 (Doroshenko et al. 2022). We emphasize that this behavior has typically been seen at luminosities far below those of the *NuSTAR* observations of EXO 2030+375 but the spectral hardening and the failure of a simple cut-off powerlaw model in Obs. II indicate a possible over-simplification of the continuum modeling.

For low-luminosity states, the complex shape of the continuum is explained by the spectral formation in an atmosphere of the neutron star, strongly overheated by direct stopping via Coulomb collisions (Sokolova-Lapa et al. 2021; Mushtukov et al. 2021). An intense redistribution near the fundamental cyclotron resonance at electron temperatures of ∼10–40 keV, results in the formation of a strong red wing of the CRSF (the effect, although less pronounced, is also well-known for electron temperatures of ∼5 keV, typically expected in accretion columns Schwarm et al. 2017; Schönherr et al. 2007). The transition from low-luminosity Coulomb braking to the matter stopping at higher luminosities is not well studied. However, in the case of a gradual transition, one can expect a similar but weaker mechanism in play at intermediate luminosities. A lack of any clear indication of a cyclotron resonance at energies above, around 30–50 keV, makes this interpretation doubtful.

Polarization effects in the strong magnetic field can also result in a complex shape of the Comptonized continuum due to the contribution of the photons of two polarization modes, which have principally different properties in interactions with electrons (Meszaros & Nagel 1985). The two modes have different spectral dependencies and a ratio of their intensities changes across the broad-band continuum, which can result in local excesses or shallow dips in a total, summed over the polarization modes, spectrum. In addition to a classical magnetized plasma, the vacuum polarization effect influences the spectral formation in the strong magnetic field (Adler 1971; Mészáros & Ventura 1978). This effect has not been investigated in greater detail for $B{\sim}10^{12}$ G, but recent advances in the field show that it is capable of enhancing the mode interchange across the spectrum and can also result in the formation of local spectral suppressions and shallow dips due to the vacuum resonance (Sokolova-Lapa et al. 2023).

5.3. Spectral evolution with pulse-phase and emission geometry

In addition to the high luminosity observations taken by various X-ray missions during the recent and historic giant outbursts, *XMM-Newton* and *NuSTAR* observed EXO 2030+375 in a low luminosity state; *XMM-Newton* at the onset of a type I outburst (Ferrigno et al. 2016) and *NuSTAR* (Fürst et al. 2017) and *AstroSAT* (Jaisawal et al. 2021) close to the propeller . These low luminosity observations are particularly interesting as EXO 2030+375 exhibited a sudden change in the photon index around $\phi \sim 0.65$[6]. While our pulse-phase binning is most likely too coarse to pick up resolve this feature, a similarly narrow drop can be seen in the hardness ratio shown in Fig. 5.

Our interpretation of the variation of the spectral parameters in terms of the emission of the accretion column is based on the relativistic ray-tracing approach discussed in further detail in Paper I. We are able to reproduce the *NICER* pulse profiles associated with the two *NuSTAR* observations with a two column model with identical columns of 2 km height and 300 m radius that emit both from the walls (fan beam) and top (pencil beam), located near the equator of the neutron star. In this model, the observed asymmetry of the pulse profiles with respect to rotational phase is due to the two columns having different emission patterns, as well as a slight displacement of the columns compared to a purely dipolar *B*-field. The evolution of the relative strengths of the peaks of the pulse profiles from one observation to the other is explained solely by a change of the emission patterns of the wall and top of each column, as well as their flux normalizations. These changes lead to an apparent phase-shift and reduction of the width of the individual sub-peaks, which when superposed cause a strong change of to the total pulse profile. The model of Paper I yields a relative decomposition of the total pulse profile into fan and pencil beam contributions of each column, so we can attempt an association of the spectral variability with the visibility of these individual components. We caution in Paper I that the full parameter space cannot be explored sufficiently to exclude other possible solutions. Uncertainty estimates on parameters are rather crude as the behavior of Markov Chain Monte Carlo (MCMC) analysis is dominated by systematic rather than statistical uncertainties. The decomposed pulse profile is shown in Figs. 7 and 8. A clear association of spectral components with emission components remains inconclusive. This is likely a result of the empirical spectral model and the oversimplified decomposition of the complex X-ray spectrum into a powerlaw and a blackbody component.

[6] Fürst et al. (2017) report this feature at phase $\phi \sim 0.85$ and Ferrigno et al. (2016) at $\phi \sim 0.27$ according to their phase definitions. Phase-matching is not entirely unambiguous due to the different pulse profile morphology at low luminosity and was done by extrapolation of the luminosity-resolved pulse profiles in Thalhammer et al. (2023) and Epili et al. (2017).

To our knowledge the only currently available radiative-transfer models for accretion columns that makes predictions of the spectral energy distribution of the radiation escaping the top of the column are those of West et al. (2017a,b, hereafter WWB17) and of Becker & Wolff (2022, herafter BW22). These authors find that in high-luminosity sources the predominant contribution to the total X-ray emission emerges from the column walls. A transition to a strong column top contribution is only expected at low mass accretion rates, far below even the fainter *NuSTAR* observation. This result is in tension with the pulse profile decomposition, which requires emission from the sides and top of the column.

As an alternative model, Postnov et al. (2015) take reflection of the relativistically downward-beamed wall emission off the neutron star surface into account that could lead to a similar emission pattern as the traditional cap or pencil component. However, in their analysis of a sample of accreting X-ray pulsars (including EXO 2030+375), the reflected component contributes substantially to a spectral hardening. Its contribution grows with increasing luminosity which implies a hardness ratio evolution with luminosity that is opposite to what we observe.

6. Conclusions & Outlook

In this work we present the broadband spectral analysis of two *NuSTAR* observations taken during the giant 2021 outburst of EXO 2030+375, once near the peak and once during the decline phase of the outburst. We find a drastic spectral transition, characterized by a spectral hardening toward lower luminosity. This hardening cannot be described by a simple change in the power-law index or folding energy but requires a more complex modification of the continuum model. This behavior is somewhat surprising as many accreting pulsars show stable powerlaw-like continuum mostly formed by Comptonized bremsstrahlung at luminosities above $10^{37}\,\mathrm{erg\,s^{-1}}$ and significant spectral transitions toward low-luminosity accretion are rather expected at luminosities at least one order of magnitude lower. Detailed radiative transfer calculations with the available column models are hampered by the unknown magnetic field strength. The only absorption feature that is robustly detected in both observations is the previously reported ∼10 keV feature. A magnetic origin is, however, highly questionable because of the lack of harmonic features which leads us to believe that this feature is a product of the complex continuum formation. The *B*-field estimate in EXO 2030+375 therefore remains an open question.

The pulse profile model presented in Paper I offers a possible emission geometry including a column wall and top component. Our attempt to associate the spectral components with these wall and top components remains somewhat inconclusive and reveals the limited physical interpretability of the traditional phenomenological spectral models. The *NuSTAR* observations and the pulse profile models raise, however, the intriguing question how the emission from the top of the column, which is strongly required by most pulse profile models (for another example, see Iwakiri et al. 2019), manifests itself in the observed X-ray spectrum. While the radiative transfer models WWB17 and BW22 includes a top emission component, its contribution is supposed to be marginal at high luminosities. Postnov et al. (2015) suggest reflected radiation from the neutron star surface as an explanation for some of the luminosity dependence of the broadband X-ray spectrum, but the behavior predicted by this model is opposite to what is seen here. A solution to these problems might be that the accretion geometry of EXO 2030+375 is more complicated than a simple skew-symmetric dipole. Such an increased accretion complexity has been proposed by Malacaria et al. (2023), based on the small polarization degree of EXO 2030+375 that was observed by *IXPE*, and is also supported by timing data of *Insight*-HXMT (Fu et al. 2023).

We expect major progress in the development of ray-tracing pulse profile models that includes reflected radiation, obscuration by the column itself, or hollow accretion column to advance our understanding of the accretion geometries in EXO 2030+375 and other X-ray pulsars. While available physically-motivated spectral models are very successful at describing the pulse-phase-averaged continuum emission at different luminosities, usable models for pulse-phase-resolved emission are not yet widely available. The deficient association of the empirical spectral evolution with the geometrical emission components underlines the need for active development in this direction. An attempt to model the pulse-phase-averged broadband X-ray spectrum of EXO 2030+375 with self-consistent hydro dynamical models such as WWB17 and a detailed study of the energy-resolved pulse profiles are outside the scope of this work and will be presented in a forthcoming publication.

Acknowledgements. We thank the *NuSTAR*, *Swift*, and *Chandra* PIs and teams for approving our DDT requests and the effort of scheduling this dense monitoring campaign. We further thank Norbert Schulz for insightful discussions of the *Chandra*/HETG spectrum. We thank the anonymous referee for useful comments and suggestions that helped to improved the manuscript. RB acknowledges support by NASA under award number 80NSSC22K0122. The material is based upon work supported by NASA under award number 80GSFC21M0002. ESL and JW acknowledge partial funding under Deutsche Forschungsgemeinschaft grant WI 1860/11-2 and Deutsches Zentrum für Luft- und Raumfahrt grant 50 QR 2202. Portions of this work performed at Naval Research Laboratory were supported by NASA. This research has made use of data from the *NuSTAR* mission, a project led by the California Institute of Technology, managed by the Jet Propulsion Laboratory, and funded by the National Aeronautics and Space Administration. Data analysis was performed using the *NuSTAR* Data Analysis Software (NuSTARDAS), jointly developed by the ASI Science Data Center (SSDC, Italy) and the California Institute of Technology (USA). This research has further made use of data obtained from the Chandra Data Archive and the Chandra Source Catalog, and software provided by the Chandra X-ray Center (CXC) in the application package CIAO.

References

Adler, S. L. 1971, Ann. Phys., 67, 599
Angelini, L., Stella, L., & Parmar, A. N. 1989, ApJ, 346, 906
Bailer-Jones, C. A. L., Rybizki, J., Fouesneau, M., Demleitner, M., & Andrae, R. 2021, VizieR Online Data Catalog, I/352
Becker, P. A. & Wolff, M. T. 2007, ApJ, 654, 435
Becker, P. A. & Wolff, M. T. 2022, ApJ, 939, 67
Bissinger né Kühnel, M., Kreykenbohm, I., Ferrigno, C., et al. 2020, A&A, 634, A99
Cash, W. 1979, ApJ, 228, 939
Doroshenko, V., Staubert, R., Maitra, C., et al. 2022, A&A, 661, A21
Epili, P., Naik, S., Jaisawal, G. K., & Gupta, S. 2017, MNRAS, 472, 3455
Ferrigno, C., Pjanka, P., Bozzo, E., et al. 2016, A&A, 593, A105
Fruscione, A., McDowell, J. C., Allen, G. E., et al. 2006, in Proc. SPIE, Vol. 6270, Observatory Operations: Strategies, Processes, and Systems, ed. D. R. Silva & R. E. Doxsey (Bellingham, WA: SPIE), 62701V
Fu, Y.-C., Song, L. M., Ding, G. Q., et al. 2023, Monthly Notices of the Royal Astronomical Society, 521, 893
Fürst, F., Kretschmar, P., Kajava, J. J. E., et al. 2017, A&A, 606, A89
Garmire, G. P., Bautz, M. W., Ford, P. G., Nousek, J. A., & Ricker, George R., J. 2003, in Society of Photo-Optical Instrumentation Engineers (SPIE) Conference Series, Vol. 4851, X-Ray and Gamma-Ray Telescopes and Instruments for Astronomy., ed. J. E. Truemper & H. D. Tananbaum (Bellingham, WA: SPIE), 28
Gendreau, K. C., Arzoumanian, Z., Adkins, P. W., et al. 2016, in Society of Photo-Optical Instrumentation Engineers (SPIE) Conference Series, Vol. 9905, Space Telescopes and Instrumentation 2016: Ultraviolet to Gamma Ray, ed. J.-W. A. den Herder, T. Takahashi, & M. Bautz (Bellingham, WA: SPIE), 99051H

Grefenstette, B., Brightman, M., Earnshaw, H. P., et al. 2022, arXiv e-prints, arXiv:2206.04058
Harrison, F. A., Craig, W. W., Christensen, F. E., et al. 2013, ApJ, 770, 103
Heindl, W. A., Coburn, W., Gruber, D. E., et al. 1999, ApJ, 521, L49
Houck, J. C. & Denicola, L. A. 2000, in Astronomical Society of the Pacific Conference Series, Vol. 216, Astronomical Data Analysis Software and Systems IX, ed. N. Manset, C. Veillet, & D. Crabtree, 591
Huenemoerder, D. P., Mitschang, A., Dewey, D., et al. 2011, The Astronomical Journal, 141, 129
Iwakiri, W. B., Pottschmidt, K., Falkner, S., et al. 2019, ApJ, 878, 121
Jaisawal, G. K., Naik, S., Gupta, S., et al. 2021, Journal of Astrophysics and Astronomy, 42, 33
Kaastra, J. S. & Bleeker, J. A. M. 2016, A&A, 587, A151
Klochkov, D., Ferrigno, C., Santangelo, A., et al. 2011, A&A, 536, L8
Klochkov, D., Horns, D., Santangelo, A., et al. 2007, A&A, 464, L45
Klochkov, D., Santangelo, A., Staubert, R., & Ferrigno, C. 2008, A&A, 491, 833
Krimm, H. A., Holland, S. T., Corbet, R. H. D., et al. 2013, ApJS, 209, 14
Lutovinov, A., Tsygankov, S., Molkov, S., et al. 2021, ApJ, 912, 17
Malacaria, C., Heyl, J., Doroshenko, V., et al. 2023, A&A, 675, A29
Meszaros, P. & Nagel, W. 1985, ApJ, 299, 138
Mészáros, P. & Ventura, J. 1978, Phys. Rev. Lett., 41
Motch, C. & Janot-Pacheco, E. 1987, A&A, 182, L55
Müller, S., Ferrigno, C., Kühnel, M., et al. 2013, A&A, 551, A6
Mushtukov, A. A., Suleimanov, V. F., Tsygankov, S. S., & Portegies Zwart, S. 2021, MNRAS, 503, 5193
Naik, S., Maitra, C., Jaisawal, G. K., & Paul, B. 2013, ApJ, 764, 158
Parmar, A. N., Stella, L., Ferri, P., & White, N. E. 1985, IAU Circ., 4066, 1
Postnov, K. A., Gornostaev, M. I., Klochkov, D., et al. 2015, MNRAS, 452, 1601
Pradhan, P., Thalhammer, P., Ballhausen, R., et al. 2021, ATel 14931
Reig, P. & Coe, M. J. 1999, MNRAS, 302, 700
Schönherr, G., Wilms, J., Kretschmar, P., et al. 2007, A&A, 472, 353
Schwarm, F.-W., Ballhausen, R., Falkner, S., et al. 2017, A&A, 601, A99
Sokolova-Lapa, E., Gornostaev, M., Wilms, J., et al. 2021, A&A, 651, A12
Sokolova-Lapa, E., Stierhof, J., Dauser, T., & Wilms, J. 2023, A&A, 674, L2
Staubert, R., Trümper, J., Kendziorra, E., et al. 2019, A&A, 622, A61
Tamang, R., Ghising, M., Tobrej, M., Rai, B., & Paul, B. C. 2022, MNRAS
Thalhammer, P., Ballhausen, R., Pottschmidt, K., et al. 2021, ATel 15006
Thalhammer, P., Ballhausen, R., Sokolova-Lapa, E., et al. 2023, A&A, submitted, (Paper I)
Tsygankov, S. S., Doroshenko, V., Mushtukov, A. A., et al. 2019a, MNRAS, 487, L30
Tsygankov, S. S., Rouco Escorial, A., Suleimanov, V. F., et al. 2019b, MNRAS, 483, L144
Verner, D. A., Ferland, G. J., Korista, K. T., & Yakovlev, D. G. 1996, ApJ, 465, 487
West, B. F., Wolfram, K. D., & Becker, P. A. 2017a, ApJ, 835, 129
West, B. F., Wolfram, K. D., & Becker, P. A. 2017b, ApJ, 835, 130
Wilms, J., Allen, A., & McCray, R. 2000, ApJ, 542, 914
Wilson, C. A., Finger, M. H., & Camero-Arranz, A. 2008, ApJ, 678, 1263
Wilson, C. A., Finger, M. H., Coe, M. J., Laycock, S., & Fabregat, J. 2002, ApJ, 570, 287